












Polymorphic chiral squaraine crystallites in textured thin films

Jennifer Zablocki¹  | Oriol Arteaga²  | Frank Balzer³  | Dirk Hertel⁴  |
 Julian J. Holstein⁵  | Guido Clever⁵  | Jana Anhäuser¹ |
 Rakesh Puttreddy⁶  | Kari Rissanen⁶  | Klaus Meerholz⁴  |
 Arne Lützen¹  | Manuela Schiek^{4,7} 

¹Kekulé Institute of Organic Chemistry and Biochemistry, University of Bonn, Bonn, Germany

²IN2UB, Department De Física Aplicada, Universitat de Barcelona, Barcelona, Spain

³Mads Clausen Institute, University of Southern Denmark, Sonderborg, Denmark

⁴Department of Physical Chemistry, University of Cologne, Cologne, Germany

⁵Faculty of Chemistry and Chemical Biology, TU Dortmund University, Dortmund, Germany

⁶Department of Chemistry, University of Jyväskylä, Jyväskylä, Finland

⁷University of Oldenburg Institute of Physics, Oldenburg, Germany

Correspondence

Prof. Dr. Manuela Schiek, Institute of Physics, University of Oldenburg, Carl-von-Ossietzky-Str. 9-11, D-26129 Oldenburg.
 Email: manuela.schiek@uol.de

Funding information

Deutscher Akademischer Austauschdienst; Ministerio de Ciencia Innovación, Grant/Award Numbers: FIS2015-73306-JIN and RTI2018-098410-J-I00 (MCIU/), RTI2018-098410- J-I00; DAAD; PRO-RETINA Stiftung; Bonn International Graduate School (BIGS); Studienstiftung des deutschen Volkes; University of Jyväskylä; Academy of Finland, Grant/Award Number: 298817; FEDER; Spanish Government

Abstract

An enantiomerically pure (*R*)-2-methylpyrrolidine-based anilino squaraine crystallizes in two chiral polymorphs adopting a monoclinic $C2$ and an orthorhombic $P2_12_12_1$ structure, respectively. By various thin-film preparation techniques, a control of the polymorph formation is targeted. The local texture of the resulting textured thin films is connected to the corresponding optical properties. Special attention is paid to an unusual Davydov splitting, the anisotropic chiroptical response arising from preferred out-of-plane orientation of the crystallites, and the impact of the polymorph specific excitonic coupling.

KEYWORDS

circular dichroism, Davydov splitting, imaging Mueller matrix polarimetry, polarized spectro-microscopy, X-ray diffraction

[This article is part of the Special Issue: In honor and memory of Prof. Koji Nakanishi. See the first articles for this special issue previously published in Volumes 31:12, 32:3, and 32:4. More special articles will be found in this issue as well as in those to come.]

This is an open access article under the terms of the Creative Commons Attribution License, which permits use, distribution and reproduction in any medium, provided the original work is properly cited.

© 2020 The Authors. *Chirality* published by Wiley Periodicals, Inc.

1 | INTRODUCTION

The advancement of organic opto-electronics relies on the development of robust organic semiconductors suitable for processing into functional thin films. Anilino squaraines are quadrupolar, donor-acceptor-donor-type small molecule semiconductors that are easily accessible via condensations reactions.¹⁻³ In the solid, they are characterized by strong intermolecular interactions mediating intense excitonic coupling with visible light,⁴⁻⁷ which renders them well suited for light harvesting and detection applications.⁸⁻¹³ Here, chiroptical properties such as excitonic circular dichroism (CD)⁷ are in the spotlight having its added value in opto-electronics in view.^{11,14,15} Polymorphism and anisotropic thin film texture,¹⁶⁻¹⁸ as well as the formation of molecular H- and J-aggregates,¹⁹⁻²² are typical features of squaraine dyes. Often two or more translationally invariant molecules are present per unit cell enabling a spectrally well-resolved Davydov splitting of the coupled molecular resonance.^{6,11,23-25} Accordingly, we found two chiral polymorphs for an enantiomerically pure (*R*)-2-methylpyrrolidine-based anilino squaraine ((*R,R*)-PyrSQ-C1), a monoclinic *C*2 and an orthorhombic *P*2₁2₁2₁ phase with two and four molecules per unit cell, respectively. In the following, we discuss the polymorph formation and anisotropic texture within thin films controlled by the solution and vapour-based processing conditions. Thereby, we focus on the local polymorph specific excitonic coupling on a microscopic scale and attempt to capture the anisotropic chiroptical response by imaging Mueller matrix polarimetry.^{26,27}

2 | MATERIALS AND METHODS

2.1 | Synthesis of 2,4-bis[4-((*R*)-2-methylpyrrolidinyl)-2,6-dihydroxyphenyl]squaraine ((*R,R*)-PyrSQ-C1)

In a single-neck flask with equipped with Dean-Stark apparatus and a reflux condenser, 5.87 mmol of (*R*)-(-)-2-methylpyrrolidine (Sigma-Aldrich, used as received) and 5.87 mmol phloroglucinol (Alfa-Aesar, used as received) were suspended in a mixture of 22 mL toluene and 22 mL 1-butanol. The reaction mixture was degassed by evacuation and flushing with argon under vigorous stirring for five cycles. The mixture was refluxed under an argon atmosphere. After 24 hours, the reaction mixture was cooled down, 2.94 mmol of squaric acid were added, and the mixture was again heated to reflux. Upon boiling, the colour of the solution turned greenish and then dark-blue within minutes. After 16 hours, the mixture was slowly cooled to room temperature and

stored at 2 °C for 1 hour to promote crystallization. The deeply coloured precipitate is collected by filtration, washed with methanol, and dried under vacuum. The raw product was further purified by a column chromatography on silica gel (gradient elution CHCl₃ → DCM). The (*R,R*)-PyrSQ-C1 anilino squaraine product was obtained as a green shiny solid.

Yield: 49%

¹H NMR: (700 MHz, CDCl₃, 298 K, δ): 11.02 (s, 4H), 5.74 (s, 4H), 4.10–4.05 (m, 2H), 3.59–3.54 (m, 2H), 3.41–3.34 (m, 2H), 2.16–2.02 (m, 6H), 1.80–1.76 (m, 2H), 1.23 (d, 6H)

¹³C NMR: (176 MHz, CDCl₃, 298 K, δ): 19.6, 22.8, 32.5, 48.6, 55.1, 94.6, 162.8, 181.5

MS (ESI+, *m/z* (%)): 464.2 (100) [M]⁺⁺, 951.4 (40) [2 M + Na]⁺

HRMS (ESI+, *m/z* (%)): [M]⁺⁺ calcd for C₂₆H₂₈N₂O₆ 464.1942, found: 464.1932

Anal. calcd. for C₂₆H₂₈N₂O₆: C 67.23, H 6.08, N 6.03; found: C 66.90, H 6.07, N 5.84

UV-vis (chloroform): λ_{max} (ε) = 647 nm (370 000 L mol⁻¹ cm⁻¹).

2.2 | Sample preparation

Thermal vapour deposition was conducted under high vacuum conditions (base pressure 1·10⁻⁷ mbar) with a deposition rate of 2 Å s⁻¹ to give thin films of 80 nm nominal thickness. As substrates, float glass microscopic slides were used for the (*R,R*)-PyrSQ-C1 thin films and were not heated during deposition. The samples were thermally annealed later on under inert glove box conditions at the indicated temperatures (hot plate surface temperature) for 90 minutes.

For the dropcasting procedure, (*R,R*)-PyrSQ-C1 was dissolved in either chloroform or toluene to give a concentration of 1 mg mL⁻¹. Droplets of these solutions were placed onto separate float glass microscopic slides, and the samples were left to dry under ambient conditions for a few hours.

To allow more insight into the preparatory conditions, we provide UV-vis and CD spectra of chloroform and toluene solutions as well as spectra of solvent-induced early stage aggregation experiments in Figure S1 of the Supporting Information (Data Set S1).

2.3 | Single crystal structure determination

2.3.1 | Monoclinic polymorph

Single crystals were grown by slow solvent evaporation from a 1 mg mL⁻¹ (*R,R*)-PyrSQ-C1 in dichloromethane.

As they only grew in extremely thin needles, synchrotron radiation was required to collect diffraction data up to atomic resolution. Data were measured at Petra III, DESY synchrotron beamline P11²⁸. A wavelength of 0.6888 Å was chosen using a liquid N₂ cooled double-crystal monochromator. Single-crystal X-ray diffraction data were collected at 80(2) K on a single-axis goniometer, equipped with an Oxford Cryostream 800 and a Pilatus 6 M detector. Seven hundred twenty diffraction images were collected in a 360° φ sweep at a detector distance of 156 mm, 100% filter transmission, 0.5° step width, and 60-millisecond exposure time per image. Data integration and reduction were undertaken using XDS.²⁹ A resolution of 0.75 Å was reached. The structure was solved by direct methods using SHELXT³⁰ and refined with SHELXL³¹ for full-matrix least squares routines on F^2 using ShelXle³² as a graphical user interface. Occupancy of the disordered methylpyrrolidine side chain was found to be 0.835(5):0.165(5) for the two conformers. Geometrical similarity for all distances of the methylpyrrolidine side chain was ensured using SADI restraints.

Crystal data: CCDC 1966422, C₂₆H₂₈N₂O₆, M = 464.50, green needle, 0.22 × 0.03 × 0.015 mm³, monoclinic, space group C2, $a = 21.095(4)$ Å, $b = 5.1030(10)$ Å, $c = 21.500(4)$ Å, $\alpha = 90^\circ$, $\beta = 109.77(3)^\circ$, $\gamma = 90^\circ$, $V = 2178.0(8)$ Å³, $Z = 4$, Dc = 1.417 g/cm³, F000 = 984, $\mu = 0.824$ mm⁻¹, $T = 171(1)$ K, $\theta_{\max} = 76.812^\circ$, 29 452 total reflections, 4358 with $I_o > 2\sigma(I_o)$, $R_{\text{int}} = 0.0392$, 5186 data, 343 parameters, 85 restraints, GooF = 1.079, $R_1 = 0.0503$ and $wR_2 = 0.1411$ [$I_o > 2\sigma(I_o)$], $R_1 = 0.0516$ and $wR_2 = 0.1429$ (all reflections), and $0.371 < d\Delta\rho < -0.312$ e/Å³, Flack = 0.0(3).

2.3.2 | Orthorhombic polymorph

Slow solvent evaporation from a saturated (*R,R*)-PyrSQ-C1 solution in a mixture of chloroform and acetonitrile resulted in single crystals of the orthorhombic polymorph suitable for X-ray structure analysis. Data were recorded by using a dual-source Rigaku SuperNova diffractometer equipped with an Atlas detector using mirror-monochromated Cu-K α ($\lambda = 1.54184$ Å) radiation.²⁸ The data collection and reduction were performed using the program *CrysAlisPro*³³, and Gaussian face index absorption correction method³³ was applied. The structure was solved using direct methods (SHELXS)^{29,30} and refined by full-matrix least squares based on F^2 using the *OLEX2* software³⁴ that utilizes the SHELXL-2015 module.^{29,30}

Crystal data: CCDC 1959607, C₂₆H₂₈N₂O₆, M = 464.50, black needle, 0.307 × 0.088 × 0.052 mm³,

orthorhombic, space group $P2_12_12_1$, $a = 8.12190(10)$ Å, $b = 11.3482(2)$ Å, $c = 23.8457(3)$ Å, $\alpha = 90^\circ$, $\beta = 90^\circ$, $\gamma = 90^\circ$, $V = 2197.83(5)$ Å³, $Z = 4$, Dc = 1.404 g/cm³, F000 = 984, $\mu = 0.824$ mm⁻¹, $T = 171(1)$ K, $\theta_{\max} = 76.812^\circ$, 29 452 total reflections, 4358 with $I_o > 2\sigma(I_o)$, $R_{\text{int}} = 0.0392$, 4600 data, 313 parameters, 0 restraints, GooF = 1.046, $R_1 = 0.0418$ and $wR_2 = 0.1126$ [$I_o > 2\sigma(I_o)$], $R_1 = 0.0442$ and $wR_2 = 0.1150$ (all reflections), $0.474 < d\Delta\rho < -0.235$ e/Å³, Flack = 0.01(7).

Crystal structures are graphed and analysed with Mercury 4.2.0.

2.4 | X-ray diffraction of thin films

X-ray diffraction (XRD) on thin films in Bragg-Brentano geometry with automatic divergence slit was performed in a PANalytical X'PertPro MPD diffractometer using Cu-K α radiation ($\lambda = 1.54184$ Å), tube set to 40 kV, and 40 mA with 10-mm beam mask. Samples were rotated in a sample spinner during measurement to eliminate possible effects from preferential in-plane orientation. XRD patterns were analysed with X'Pert HighScore Plus 3.0.5.

2.5 | Microscopic and spectroscopic thin film characterization

Atomic force microscopy (AFM) was performed with a JPK NanoWizard in intermittent contact mode (Budget Sensors Tap-300G, resonance frequency 300 kHz, force constant 40 N/m) under ambient conditions and in combination with an inverted optical microscope (Nikon Eclipse TE 300). Spatially resolved, polarized absorbance spectra were taken by an Ocean Optics Maya 2000 miniature spectrometer, coupled via a 200- μ m optical fibre to the camera port of a Leica DM RME metallographic microscope. For this, the sample was mounted on a computer controlled rotation stage (Thorlabs PRM1Z8) and illuminated by a light-emitting diode light source. On a larger scale, polarization resolved reflection and transmission microscope images (PixeLINK PL-B873-CU) were taken either with white light illumination, or through appropriate interference filters at fixed wavelengths. From an analysis of the intensity variation with sample rotation angle, the direction of maximal transmission and reflection was extracted for each image pixel.^{35,36}

In addition, microscopy images between crossed polarizers have been recorded with an Olympus BX41 in reflection equipped with a DP12 digital camera.

Macroscopic (2-mm illumination spot diameter) UV-vis spectra as well as intensity normalized nine-element Mueller Matrix recordings in transmission have been

obtained with a Woollam VASE spectroscopic ellipsometer.⁷ The matrix logarithm of the Mueller matrix completed by symmetry considerations has been calculated, and the CD has been extracted as the average of log-M04 and log-M40 elements. CD is twice the values of ellipticity for small quantities. See Schulz et al⁷ for full explanation.

2.6 | Imaging Mueller matrix polarimetry

Imaging Mueller matrix measurements with microscopic resolution have been obtained with a custom made instrument.²⁷ This Mueller matrix microscope was coupled to a monochromator for spectroscopic Mueller matrix imaging measurements. Measurements were made with two different magnifications provided by Carl Zeiss 10× and 50× microscope objectives. When the 50× objective was employed, the polarization state analyser of the microscope was removed in order to maximize light intensity (ie, measurements were made only with the polarization state analyser). In this configuration, the instrument measures the first row of the Mueller matrix and CD was assimilated to the M04 Mueller matrix element (as it is done in commercial CD spectropolarimeters).

3 | RESULTS AND DISCUSSION

3.1 | Polymorphic crystal structures

The enantiomerically pure (*R,R*)-PyrSQ-C1 has been obtained via a sequential one-pot-two-step chiral pool condensation reaction. Crystals suitable for structure determination have been obtained by solution-assisted growth. Two different crystal forms could be resolved: a monoclinic *C2* polymorph and an orthorhombic $P2_12_12_1$ polymorph. Their chiral unit cell parameters are listed in Table 1. The molecular packing viewing from various orientations is shown in Figures 1 and 2 for monoclinic and orthorhombic polymorph, respectively. Surely, the flexibility of the orientation of the methyl groups at the pyrrolidine rings supports the polymorphism.

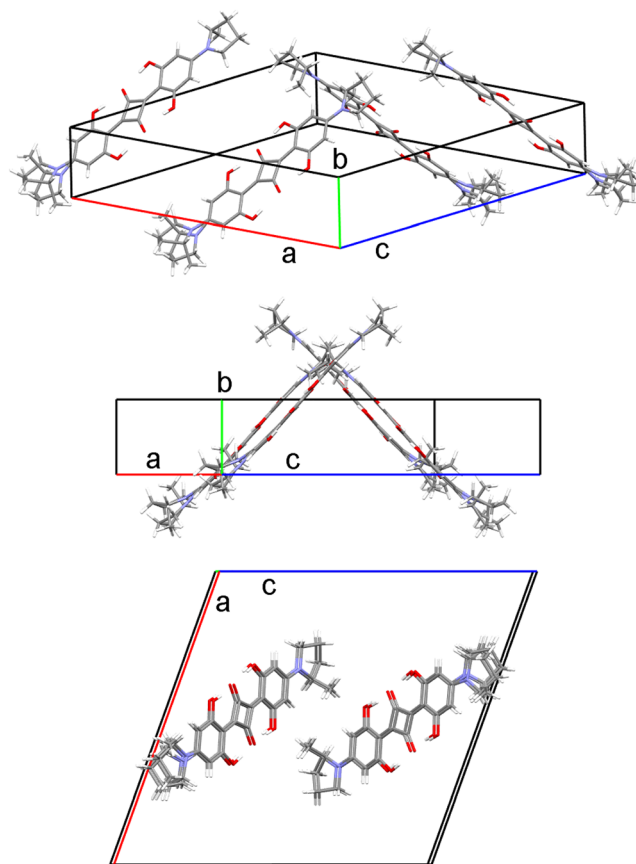


FIGURE 1 Molecular packing of the monoclinic (*R,R*)-PyrSQ-C1 polymorph (*C2*) containing two molecules per unit cell

Within the *C2* polymorph, the two squaraine molecules within the unit cell adopt a conformation with a *trans*-arrangement of the methyl groups relative to the conjugated backbone leading to an up-up orientation of these groups. This causes a certain wavy shape of the molecule; ie, it is not fully coplanar along the conjugated backbone. However, approximately 15% of the pyrrolidine rings are found to be disordered leading to a *cis* conformation with up-down orientation of the methyl groups. A herringbone packing is visible viewing along the [100] direction with an angle of about 85° (Figure 1, middle). Molecular stacking is along the crystallographic *b* direction (Figure 1, bottom).

The $P2_12_12_1$ polymorph contains four molecules per unit cell, which have a fully coplanar conjugated backbone. Here, the molecules adopt a conformation with a *cis* arrangement of the methyl groups relative to the

TABLE 1 Unit cell parameters of (*R,R*)-PyrSQ-C1 polymorphs

Polymorph	<i>a</i> , Å	<i>b</i> , Å	<i>c</i> , Å	β , °	<i>Z</i>
<i>C2</i> monoclinic	21.095(4)	5.1030(10)	21.500(4)	109.77(3)	2
$P2_12_12_1$ orthorhombic	8.12190(10)	11.3482(2)	23.8457(3)	90	4

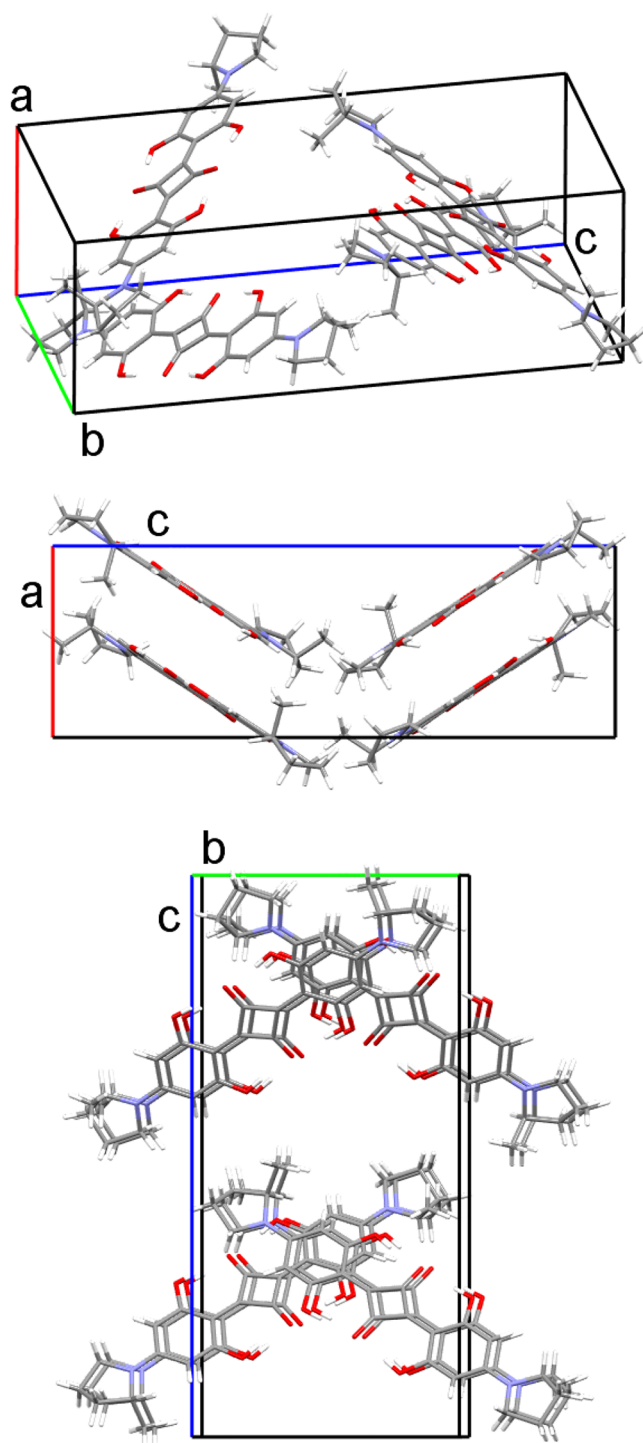


FIGURE 2 Molecular packing of the orthorhombic (*R,R*)-PyrSQ-C1 polymorph ($P2_12_12_1$) containing four molecules per unit cell

conjugated backbone leading to an up-down orientation of the methyl groups. A herringbone packing is visible viewing along the [010] direction with a flatter herringbone angle of about 117° (Figure 2, middle). The molecular stacking is along the crystallographic *a* direction consisting of two interdigitating molecular stacks. The tilt

angle between these two stacks is about 3° , while the molecules are coplanar within a single stack. They are rotated about 115° against each other (Figure 2, bottom).

Such a formation of polymorphs and their molecular packing motif is very similar to the crystallization observed for *N,N*-diisobutyl anilino squaraine (SQIB).¹⁶ There, the monoclinic and orthorhombic SQIB polymorphs crystallize in centrosymmetric space groups with $P21/c$ and $Pbcn$ unit cells, respectively. This packing motif is principally different from *N,N*-di-*n*-alkyl anilino squaraines typically crystallizing into a triclinic $P-1$ unit cell containing only a single molecular organization into π -stacks.^{22,37}

3.2 | Vapour-deposited samples

Thermal vapour deposition in high vacuum of (*R,R*)-PyrSQ-C1 on a glass substrate without substrate heating gives continuous, amorphous thin films. Here, samples with an initial layer thickness of 80 nm are discussed. Postannealing of such samples induces crystallization into the monoclinic polymorph with a preferred out-of-plane orientation. In Figure 3A, XRD patterns of thin films as-deposited and postannealed at 100, 140, and 180°C , respectively, are displayed. The evolution of a single peak indicative for the (100) plane of the monoclinic polymorph being parallel to the surface shows an increasing degree of crystallinity with rising annealing temperatures. Note that only the (200) peak is visible due to systematic extinction of (*h*00) peaks for odd *h*. Further rise of temperature causes evaporation of the organic material. The grainy texture and a certain bireflectance of a sample annealed at 180°C is visible in a microscopy image between crossed polarizers, Figure 3B. A sketch of the view onto the monoclinic (100) plane is displayed in Figure 3C.

Spectroscopic characterization of the samples is conducted in normal incidence transmission, ie, with view on the (100) face. For the non-annealed thin film, the absorbance spectrum has a similar appearance compared with the (*R,R*)-PyrSQ-C1 in chloroform solution. Yet, it is clearly red-shifted and the maximum is located at 665 nm (instead of 647 nm in solution) with a vibronic sideband at 610 nm (Figure 4A). However, the spectrum indicates a random (amorphous) arrangement of the molecules; no signatures of Frenkel excitonic coupling are noticeable. For the annealed samples, the spectral course changes (Figure 4A). The spectrum broadens and a Davydov splitting becomes noticeable typical for molecular aggregation and formation of Frenkel excitonic coupling with oblique/chiral molecular alignment.³⁸ The peak maxima for the Upper Davydov Component (UDC) and the Lower

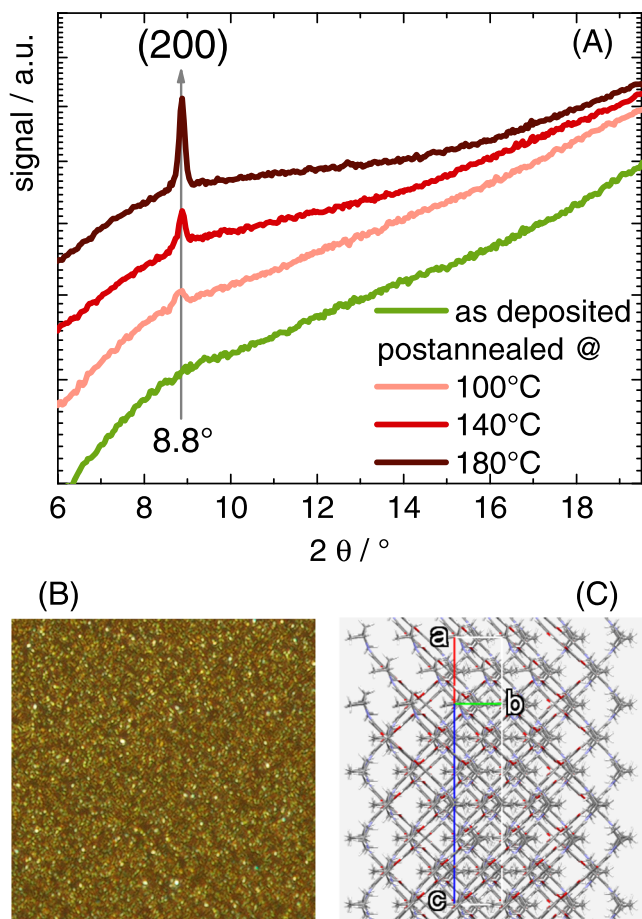


FIGURE 3 A, X-ray diffraction patterns of vapour-deposited (*R,R*)-PyrSQ-C1 thin films with nominal film thickness of 80 nm, later on annealed at the indicated temperatures. B, Microscopy image between crossed polars of (*R,R*)-PyrSQ-C1 thin film postannealed at 180 °C, image size $50 \times 50 \mu\text{m}^2$. C, Sketch of molecular packing including unit cell axes of the monoclinic 2 polymorph with view onto the (100) crystal face

Davydov Component (LDC) are located at 580 and 660 nm, respectively, for 100 °C annealing. This gives a splitting energy of 260 meV. Both peaks red-shift for increased annealing at 140 °C to 590 and 670 nm (250 meV splitting energy). The spectrum broadens for annealing at 180 °C with the LDC further shifting to 700 nm, while the UDC remains at 590 nm but with less markedness. Davydov splitting energy increases to 330 meV.

In Figure 4B, the CD spectra of the samples extracted from Mueller matrix recordings as explained in detail in Schulz et al⁷ are displayed. Unfortunately, the CD response is insignificant. Signals are on the order of instrumental noise level. Also, the spatially resolved imaging Mueller matrix polarimetry inspection of the samples could not detect any considerable CD response. This is expected for the amorphous thin film due to the absence of distinct excitonic molecular coupling.⁷ For

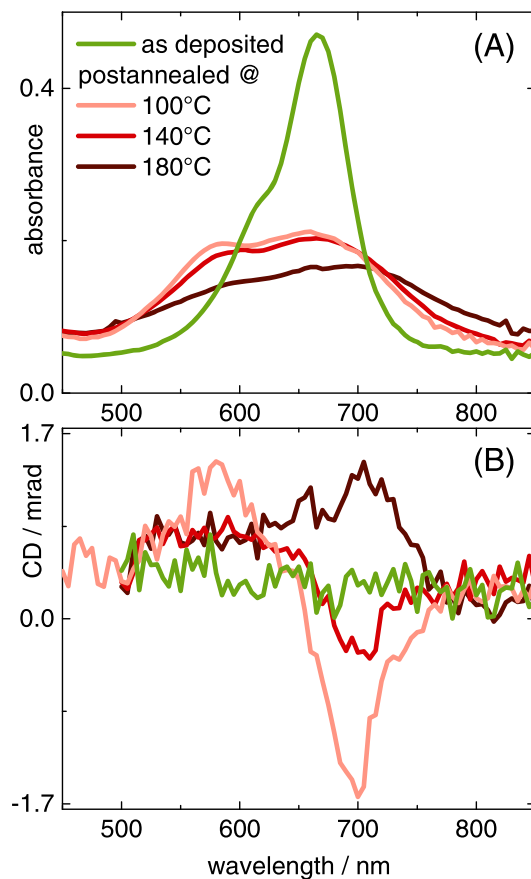


FIGURE 4 A, Absorbance spectra of vapour deposited (*R,R*)-PyrSQ-C1 thin films with nominal film thickness of 80 nm, later on annealed at the indicated temperatures. B, Corresponding circular dichroism spectra

this microcrystalline thin films of (*R,R*)-PyrSQ-C1, the CD response is anisotropic.^{39,40} The optical activity tensor α for a monoclinic crystal with space group *C*2 has the following non-diagonal form:

$$\alpha = \begin{bmatrix} \alpha_{11} & \alpha_{12} & 0 \\ \alpha_{21} & \alpha_{22} & 0 \\ 0 & 0 & \alpha_{33} \end{bmatrix}. \quad (1)$$

We consider the Tellegen constitutive equations for optical activity⁴¹ that can be casted in matrix form as follows:⁴²

$$\begin{bmatrix} \mathbf{D} \\ \mathbf{B} \end{bmatrix} = \begin{bmatrix} \epsilon & i\alpha \\ -i\alpha^T & \mu \end{bmatrix} \begin{bmatrix} \mathbf{E} \\ \mathbf{H} \end{bmatrix}, \quad (2)$$

where \mathbf{E} and \mathbf{H} are the electric and magnetic field vectors and \mathbf{D} and \mathbf{B} are the corresponding electric displacement and magnetic induction, respectively; ϵ and μ are the permittivity and permeability tensors.

For the studied (100) crystal face and in first-order approximation, the measured CD under normal incidence scales with the optical activity tensor components such as $CD_{(100)} \propto (\alpha_{22} + \alpha_{33})$. In case α_{22} and α_{33} are close to zero, or $\alpha_{22} \approx -\alpha_{33}$, the (100) face of the monoclinic polymorph gives a vanishing CD signal, in accordance with the experimental data. We can constitute at this stage that the (100) crystal face of the monoclinic polymorph is CD-silent.

3.3 | Dropcasted samples

Solubility of the (*R,R*)-PyrSQ-C1 is too low and its liability to crystallize too high for solution processing by spin-coating to give continuous films. For dropcasting from toluene, concomitant polymorphs both with a single preferred out-of-plane orientation grow. The XRD pattern in Figure 5 (lower curve) shows the (100) crystal face

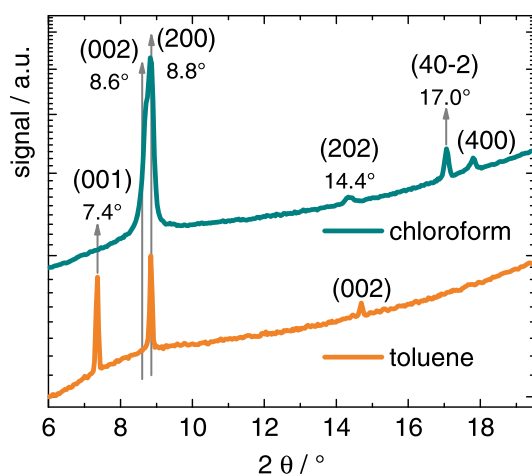


FIGURE 5 X-ray diffraction patterns of dropcasted (*R,R*)-PyrSQ-C1 from chloroform solution (upper pattern) and toluene solution (lower pattern)

parallel to the surface for the monoclinic phase and (001) face for the orthorhombic phase. Dropcasting from chloroform results in the formation of the monoclinic polymorph only but with multiple orientations. From the XRD pattern (Figure 5 upper curve), (100), (001), (101), and (20-1) crystal faces parallel to the surface can be identified. The (100) orientation seems to dominate since there is also a second order diffraction peak visible. However, all orientations have in common that the molecular stacking direction being along the crystallographic *b*-axis runs parallel to the surface. Here, the *b*-axis is the unique axis of the monoclinic unit cell; thus, the two-fold rotation axis is parallel to the molecular stacking direction. Driving force for the orientation are the strong intermolecular interactions typical for squaraines, only for highly templating metallic surface a wetting layer with non-stacking molecules was found.⁴³

3.3.1 | Dropcasting from chloroform

Microscopic inspection of the chloroform samples shows the formation of drying fringes containing crystallites with various shapes, Figure 6A. Their bireflection makes them visible between the crossed polars of the microscope. At the lower rims of such fringes, lamella-like crystallites emerge. Their shape is resolved by AFM as shown in Figure 6B. They are a few hundreds of nanometres high, but they are transparent enough to perform local optical transmission spectroscopy. A representative absorbance spectrum of a lamella-like crystallite is depicted in Figure 7A (cyan curve). It shows a Davydov splitting very similar to the postannealed vapour-deposited thin films, but the peak maxima are slightly shifted to 575 nm (UDC) and 650 nm (LDC) giving a splitting energy of 250 meV.

Imaging Mueller matrix polarimetry reveals a significant CD response as shown in Figure 7A (black curve).

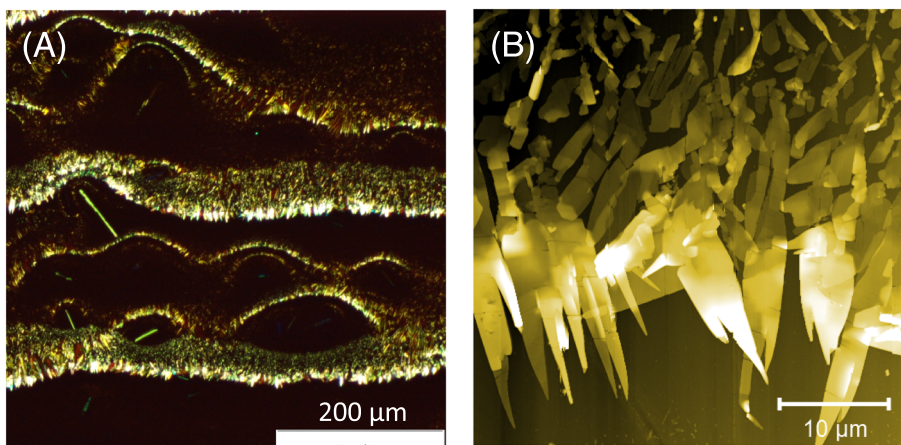


FIGURE 6 A, Microscopy image between crossed polarizers of dropcasted (*R,R*)-PyrSQ-C1 from chloroform solution. B, Atomic force microscopy image (intermittent contact mode) of monoclinic lamella-like crystallites at the outer rim of a drying fringe. Image size $40 \times 40 \mu\text{m}^2$ and height scale 400 nm

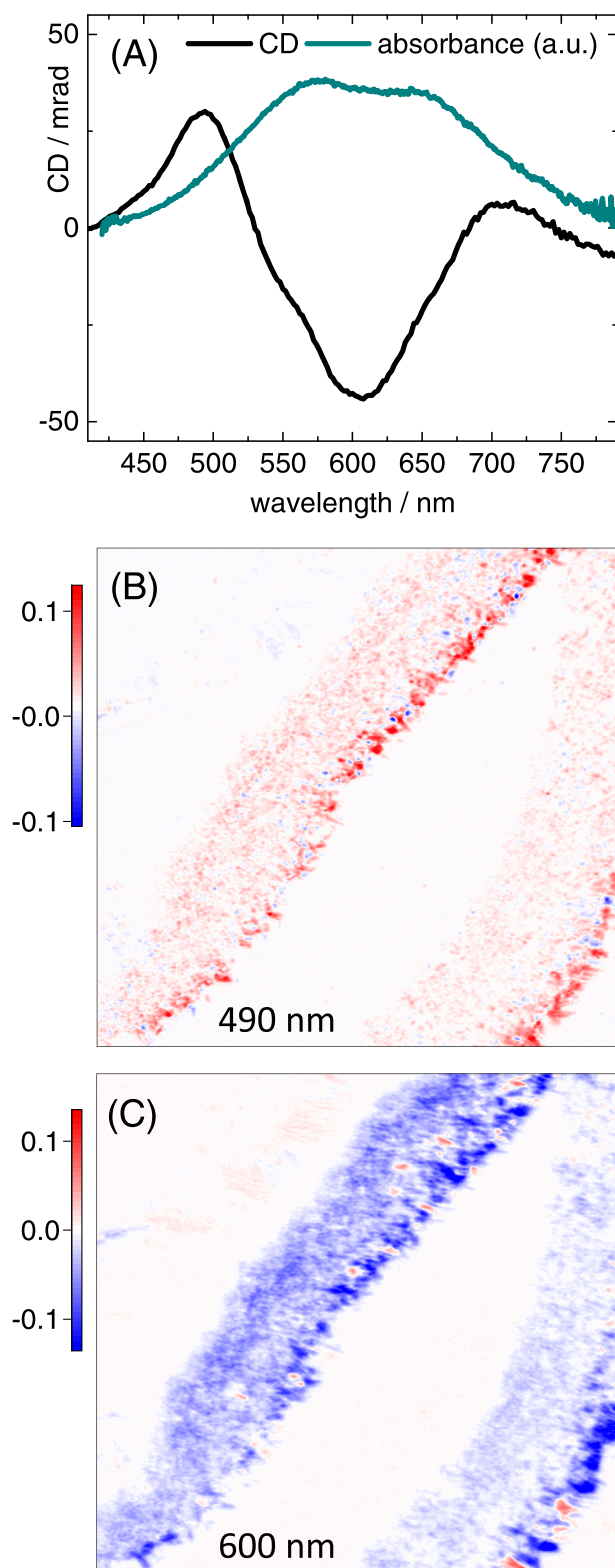


FIGURE 7 A, Local absorbance and circular dichroism (CD) spectra of lamella-like (*R,R*)-PyrSQ-C1 crystallites grown by dropcasting from chloroform. The 2D-plots in (B) and (C) show a spatially resolved CD response at 490 nm (B) and 600 nm (C), respectively, recorded by imaging Mueller matrix polarimetry (image size $330 \times 248 \mu\text{m}^2$). The same sample area is imaged in (B) and (C)

The spectral shape is complex consisting of two positive lobes and a negative lobe with a minimum at 600 nm and a maximum at 490 nm. Bisignate signals and superpositions thereof are typical for excitonic CD spectra.^{7,44} As a further indication for an excitonic CD response, the spectral integral approaches zero.⁴⁵ The dissymmetry factor, defined as differential absorbance divided by unpolarized absorbance, can be estimated to be on the order of 10^{-2} for the minimum CD at 600 nm. The CD response at 490 and at 600 nm is imaged spatially resolved in Figures 7B and 7C, respectively. It can be seen that only the lamella-like crystallites at the outer rim of a drying fringe give a distinct CD response. The CD signal clearly is positive at 490 nm (Figure 7B) and negative at 600 nm (Figure 7C). Thus, these monoclinic lamella-like crystallites adopt a different orientation with respect to the surrounding (*R,R*)-PyrSQ-C1 material. We can exclude the (100) orientation, because this crystal face appeared to be CD-silent in the characterization of the postannealed vapour-deposited thin films. According to Equations (1) and (2) and in first-order approximation, the CD response measured under normal incidence scales as follows with the three other realized crystallographic orientations: $\text{CD}_{(001)} \propto (\alpha_{11} + \alpha_{22})$, $\text{CD}_{(101)} \propto (0.5 \cdot \alpha_{11} + 0.5 \cdot \alpha_{33} + \alpha_{22})$, and $\text{CD}_{(20-1)} \propto (0.11 \cdot \alpha_{11} + 0.89 \cdot \alpha_{33} + \alpha_{22})$.

However, for now, it remains elusive which of these crystal faces, that are (001), (101) or (20-1), is the most CD-active and is adopted by the CD-active, lamella-like crystallites.

3.3.2 | Dropcasting from toluene

In case of dropcasting from toluene, the assignment of polymorph and orientation is straightforward (Figure 8A). Additional scanning electron microscopy images of such aggregates can be found in Figure S2 in the Supporting Information (Data Set S1). The fuzzy blue-greenish crystals consist of the monoclinic polymorph with (100) orientation. Also here, they appear CD-silent in imaging Mueller matrix polarimetry investigation. The brick-like shiny golden crystallites are made of the orthorhombic polymorph with (001) alignment. The quasimetallic shine is indicative for strong intermolecular interactions.⁴⁶ The bricks vary a lot in thickness from about 150 nm to more than a micrometer. An AFM image of a small brick ($200 \text{ nm} \times 20 \mu\text{m}$) is displayed in Figure 8B revealing its very flat surface. This thin brick is suitable for optical spectroscopy in transmission. Its polarized spectro-microscopy recordings are representative since all bricks show a characteristic linear dichroism (LD). Selected linear polarized absorbance spectra of this brick are shown in Figure 8C. For the linear polarized

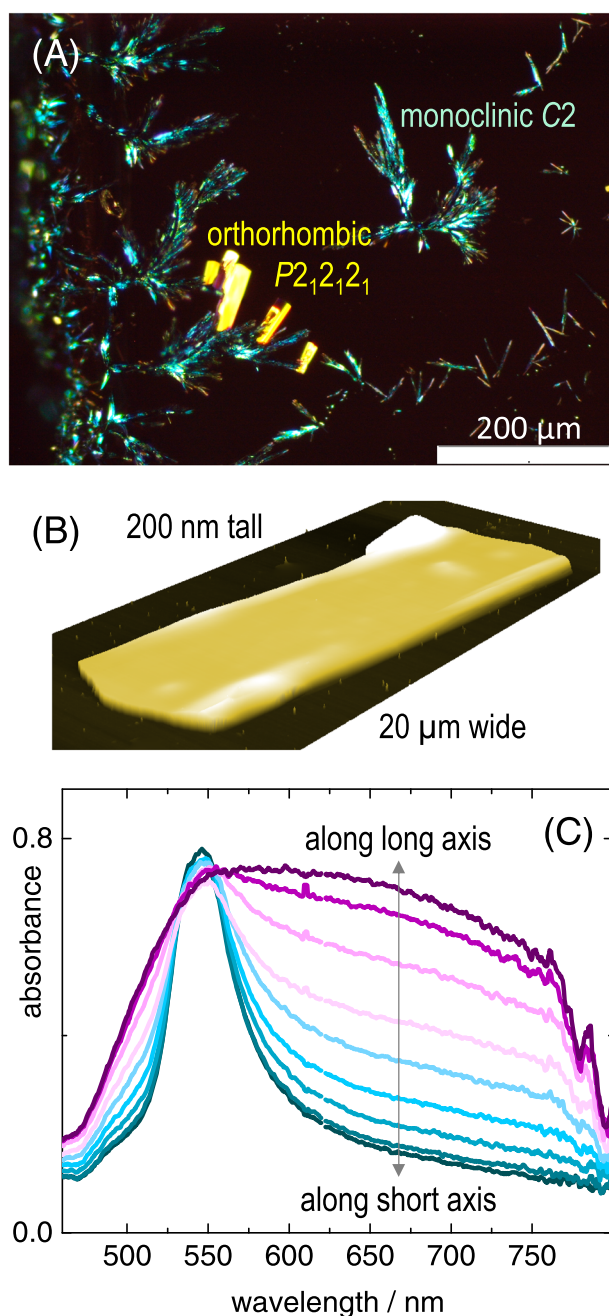


FIGURE 8 A, Microscopy image between crossed polarizers of dropcasted (*R,R*)-PyrSQ-C1 from toluene solution showing concomitant monoclinic (green-bluish) and orthorhombic crystallites (shiny golden). B, Atomic force microscopy image (intermittent contact mode) of orthorhombic shiny golden brick-like crystallites. C, Linear polarized absorbance spectra of such a brick-like crystallite recorded for 90° azimuthal rotation of the polarizer with transmission axis from parallel (lilac) to perpendicular (cyan) to long brick axis

absorbance along the long brick axis, the spectrum is very broad ranging from approximately 500 to 780 nm (lilac curve in Figure 8C). The absorbance polarized along the short brick axis is rather sharp with a clear peak at

545 nm (cyan curve in Figure 8C). This behaviour is remarkable and demands further theoretical studies to explain the spectral course.

In the Supporting Information, three movies of the brick shown in Figure 8B can be found: MOV_1 (Movie S1) rotated between crossed polars (reflection) and MOV_2 (Movie S2) and MOV_3 (Movie S3) rotated with a single polarizer in the reflected and transmitted beam, respectively (unpolarized illumination).

An analysis of these image stacks by a discrete Fourier transform delivers—spatially resolved—the directions of maximal reflection and transmission as well as the extinction^{35,36}(Figure 9). Maximum reflectivity is obtained when the long axis of the brick is parallel to the polarizer direction, whereas the maximum transmission is obtained for light polarized perpendicular to the long brick axis. The polarization directions for maximal extinction between crossed polars are parallel as well as perpendicular to the long brick axis.

From this, we can find a structural model for the molecular alignment based on simple exciton theory.^{14,41,47}The out-of-plane orientation is known from XRD measurements to be (001). Typically, molecular stacking is along the short unit cell axis, which renders the crystallographic *a*-axis to be aligned along the long brick axis. A sketch based on the orthorhombic single crystal structure is shown in Figure 10A. The transition dipole moment (TDM) for anilino squaraines is usually along the long molecule axis as sketched in Figure 10B. In a molecular dimer Frenkel exciton picture with oblique orientation graphical vector addition of the molecular TDMs can be used to calculate the *x*- and *y*-components of the excitonic TDMs¹⁴ (Figure 10B). Here, the *x*-component resembles the LDC or J-like component with red-shifted transition energy. Likewise, the *y*-component gives the UDC or H-like component with blue-shifted transition energy.⁴⁷ For graphical vector addition of the projected TDM as sketched in Figure 10A, the *x*-component is along the long brick axis and the *y*-axis is along the short brick axis. This fits reasonable to the remarkably broad absorbance (J-like *x*-component) along the long brick axis, as well as to the sharp, bluish absorbance (H-like *y*-component) along the short brick axis. Thus, we have resolved a complete picture of molecular as well as linear excitonic TDM orientation for the orthorhombic brick-like crystallites.

Finally, we are able to detect a circular dichroic response from the bricks by local, spatially resolved imaging Mueller matrix polarimetry, see Figure 11. For these transmission measurements, the light beam propagates along [001], ie, one of the three twofold screw axes, which are parallel to the crystallographic axes. Since for orthorhombic crystals the indicatrix of the optical activity

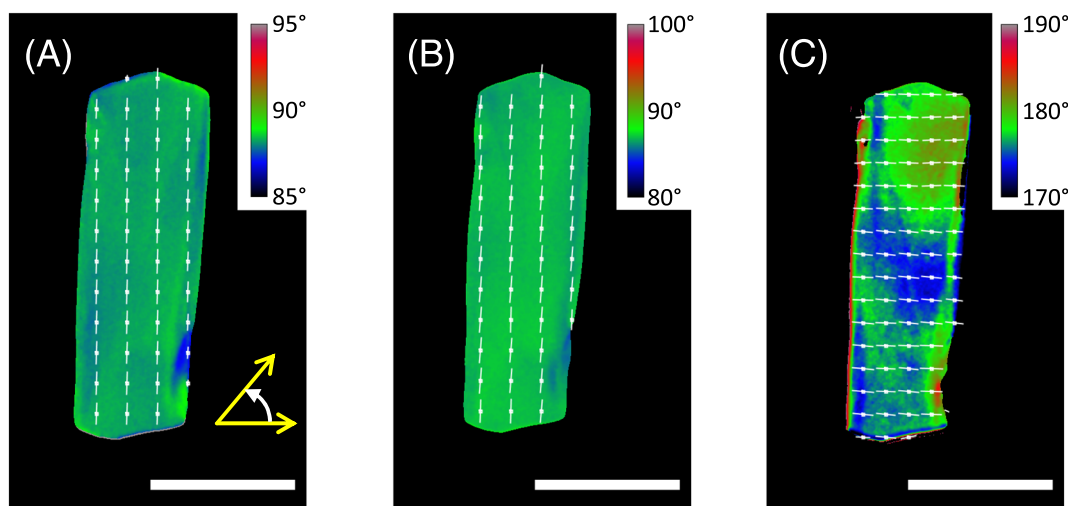


FIGURE 9 Spatially resolved polarization analysis of the brick shown in Figure 8b (scale bars 20 μm). The polarizer directions for maximum extinction between crossed polarizers (A), single polar maximum reflection (B), and maximum transmission (C) are colour encoded and depicted by the white lines

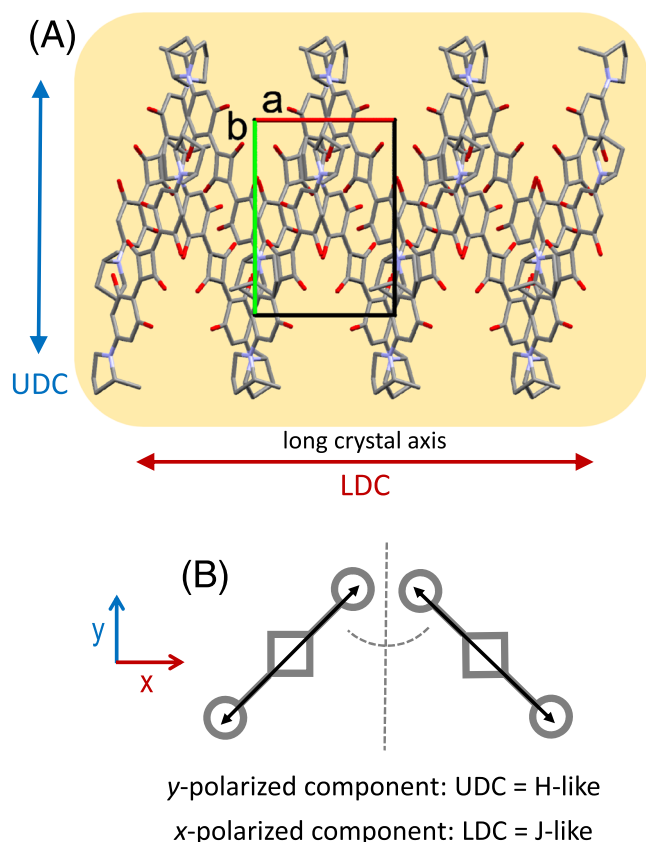


FIGURE 10 A, Structural model for the molecular and excitonic transition dipole moment (TDM) alignment within the orthorhombic brick-like crystallites. B, Molecular dimer picture in a simple Frenkel exciton model. The molecular TDM is along the long molecular axis. The x - and y -polarized excitonic components are calculated by graphical vector addition. For the structural model in (A) this means that Upper Davydov Component is polarized along the short brick axis while Lower Davydov Component is polarized along the long brick axis

tensor is congruent with the crystallographic axes,⁴⁸ a CD response is expected along the inspected direction. The optical activity tensor of an orthorhombic crystal has therefore the following diagonal form:

$$\boldsymbol{\alpha} = \begin{bmatrix} \alpha_{11} & 0 & 0 \\ 0 & \alpha_{22} & 0 \\ 0 & 0 & \alpha_{33} \end{bmatrix} \quad (3)$$

According to Equation (2), the measured CD for normal incidence on the (001) face scales as $\text{CD}_{(001)} \propto (\alpha_{11} + \alpha_{22})$. Given the complexity of the tensor, even for this diagonal form, a measurement on a single-crystal face is not sufficient to obtain information on the specific values of the tensor components.

Figures 11b-11d display the CD topography of three neighbouring bricks tagged by the numbers 1, 2, and 3 at three selected wavelengths. The rough CD spectral course of brick 1 is plotted in Figure 11A. It reveals spectral signatures, which are not resolved in the linear polarized absorbance spectra (Figure 8C). We find the sign of CD to change within a narrow spectral range. For brick 1, CD is positive at 618 nm (Figure 11B), negative at 623 nm (Figure 11C), and positive at 630 nm (Figure 11D). This is the predominant case; ie, this is the response of thinner bricks consisting of (*R,R*)-PyrSQ-C1 in a (001) orientation. For thicker bricks, such as brick 3, the polarimetric measurements are severely impaired by imaging artefacts. In a particular case, brick 2, we found the CD response to be of opposite course compared with brick 1. Possible reasons for this mirrored spectral shape are either a crystallite made up of the other

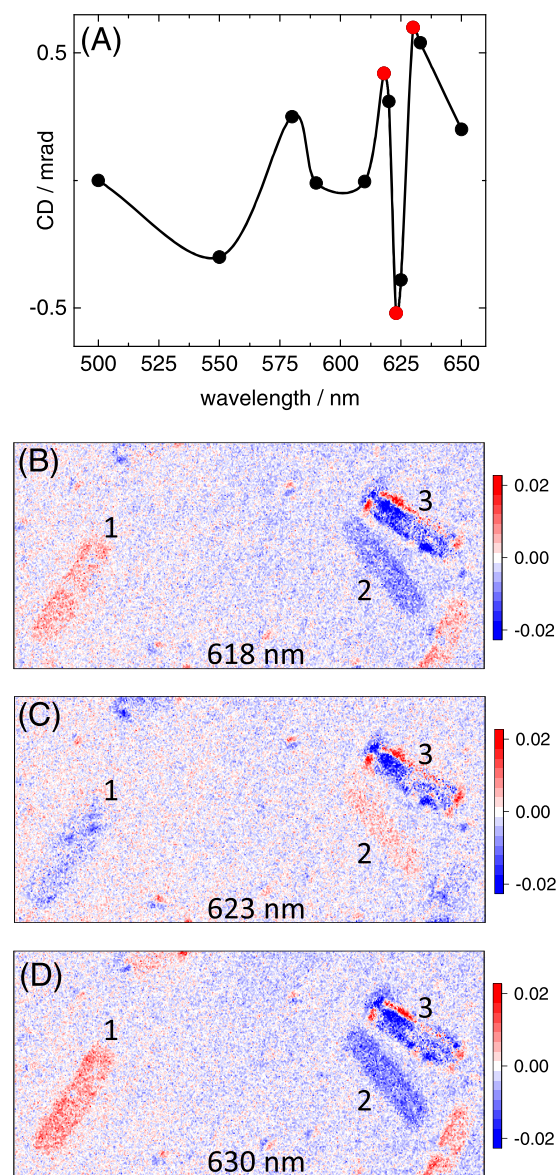


FIGURE 11 In (A), the local circular dichroism (CD) response of brick 1, as indicated in the following 2D graphs, is plotted for selected wavelengths. The solid B-spline curve is to guide the eye. For the spectral positions marked in red, the spatially resolved CD response is shown displaying three different bricks at 618 nm (B), 623 nm (C), and 630 nm (D), respectively. The 2D scans are obtained by imaging Mueller matrix polarimetry (image size $248 \times 180 \mu\text{m}^2$). Note the opposite spectral course of brick 2 (rare case) compared with brick 1 (typical). The thicker brick 3 shows imaging artefacts due to sensitivity limitations imposed by the high magnification optical imaging

enantiomer or a different crystallographic orientation of an (*R,R*)-enantiomer crystallite. This could be the (010) orientation, which would hardly be noticeable in XRD inspection due to low scattering probability. The CD response for this crystal face would according to Equations (2) and (3) scale as $\text{CD}_{(010)} \propto (\alpha_{11} + \alpha_{33})$. However, at

this stage, we cannot draw further conclusions here. Quantum chemical calculations would provide a further insight and are therefore highly desired for future collaborative work. So far, the observed sign changes of CD in a narrow spectral range, where all the other optical properties remain approximately constant, suggest that the measured CD is a true signal despite the sensitivity limitations imposed by the high magnification optical imaging. This is further supported by the “lucky find” of a crystallite (brick 2) that systematically shows an opposite optical activity from all other imaged bricks.

4 | CONCLUSION

We have found two chiral polymorphs for the pyrrolidine-based anilino squaraine (*R,R*)-PyrSQ-C1, adopting a packing motif that is, apart from being chiral, strikingly similar to a fully symmetric anilino squaraine with iso-butyl side chains. We can control the polymorph formation by solution- and vapour-based processing conditions to give textured thin films. In case of using rather noninteracting glass substrates, the molecular interactions are dominant, which causes the molecular stacking directions to run parallel to the surface for all realized orientations. The CD response is highly anisotropic, so that we could only find a significant CD signal for one of the preferred orientations of the monoclinic polymorph. However, an assignment of the crystallographic orientation is still pending. The orthorhombic polymorph is very attractive because of its strong excitonic coupling leading to an amazing LD response. The combination of XRD and polarized spectro-microscopy enabled us to obtain a full picture of molecular and linear excitonic TDMs. We anticipate a likewise remarkable enhancement of the CD response, yet highly depending on the inspected crystal face. So far, the polarimetric measurements have been cumbersome and need to be improved to reveal the full potential of the material. However, we could already identify a true optical activity hinting to additional spectral signatures that have not been resolved in the linear polarized measurements. Further understanding of the complete linear and circular dichroic properties for fundamental curiosity reasons asks for theoretical considerations, which will be part of future collaborative work. This will inspire the design of novel chiroptical applications.

ACKNOWLEDGMENTS

M. S. thanks the DAAD for a travel grant to the CD2019 and their organizers and contributors for an inspiring conference, the “PRO-RETINA Stiftung” for funding, and Prof. em. Jürgen Parisi for providing infrastructure and

technical support (Ulf Mikolajczak). O. A. thanks the Spanish Government and FEDER fund for financial support (FIS2015-73306-JIN and Ministerio de Ciencia Innovación RTI2018-098410- J-I00 (MCIU/AEI/FEDER, UE)). R. P. and K. R. gratefully acknowledge financial support from the Academy of Finland (RP grant no. 298817) and the University of Jyväskylä, Finland. J. A. thanks the “Studienstiftung des deutschen Volkes” for a doctoral grant and the Bonn International Graduate School (BIGS) for a travel grant. Diffraction data of the monoclinic polymorph was collected at PETRA III at DESY, a member of the Helmholtz Association (HGF). The authors thank Olga Lorbeer for assistance in using synchrotron beamline P11 (I-20180412), Dr. Daniele Fazzi (University of Cologne) for discussion on quantum chemical aspects, and Ruth Bruker (University of Cologne) for recording the SEM images.

FUNDING INFORMATION

PRO-RETINA Stiftung, DAAD (travel grant for M. S.), FIS2015-73306-JIN and Ministerio de Ciencia Innovación RTI2018-098410- J-I00 (MCIU/AEI/FEDER, UE), Academy of Finland (RP grant no. 298817), Studienstiftung des deutschen Volks (PhD grant for J. A.), Bonn International Graduate School (BIGS) (travel grant for J. A.).

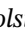
ORCID

Jennifer Zablocki  <https://orcid.org/0000-0002-2100-4807>

Oriol Arteaga  <https://orcid.org/0000-0001-9015-0237>

Frank Balzer  <https://orcid.org/0000-0002-6228-6839>

Dirk Hertel  <https://orcid.org/0000-0002-0421-9734>

Julian J. Holstein  <https://orcid.org/0000-0002-8385-7805>

Guido Clever  <https://orcid.org/0000-0001-8458-3060>

Rakesh Puttreddy  <https://orcid.org/0000-0002-2221-526X>

Kari Rissanen  <https://orcid.org/0000-0002-7282-8419>

Klaus Meerholz  <https://orcid.org/0000-0001-7450-4672>

Arne Lützen  <https://orcid.org/0000-0003-4429-0823>

Manuela Schiek  <https://orcid.org/0000-0002-0108-2998>

REFERENCES

- Sreejith S, Carol P, Chithra P, Ajayaghosh A. Squaraine dyes: a mine of molecular materials. *J Mater Chem*. 2008;18:264-274.
- Beverina L, Sassi M. Twist and turns around a square: the many faces of squaraine chemistry. *Synlett*. 2014;25:477-490.
- Irina K, MacCuaig WM, Laramie M, Jeouty JN, McNally LR, Henary M. Squaraine dyes: molecular design for different applications and remaining challenges. *Bioconjug Chem*. 2019;31(2):194-213. <https://doi.org/10.1021/acs.bioconjugchem.9b00482>
- Tristani-Kendra M, Eckhardt C, Bernstein J, Goldstein E. Strong coupling in the optical spectra of polymorphs of a squarylium dye. *Chem Phys Lett*. 1983;98:57-61.
- Röhr MIS, Marciniak H, Hoche J, et al. Exciton dynamics from strong to weak coupling limit illustrated on a series of squaraine dimers. *J Phys Chem C*. 2018;122:8082-8093.
- Sanyal S, Painelli A, Pat SK, Terenziani F, Sissa C. Aggregates of quadrupolar dyes for two-photon absorption: the role of intermolecular interactions. *Phys Chem Chem Phys*. 2016;18(40):28198-28208.
- Schulz M, Zablocki J, Abdullaeva OS, et al. Giant intrinsic circular dichroism of prolinol-derived squaraine thin films. *Nat Commun*. 2018;9:2413.
- Law KY. Squaraine chemistry. Design, synthesis, and xerographic properties of a highly sensitive unsymmetrical fluorinated squaraine. *Chem Mater*. 1992;4:605-611.
- Chen G, Sasabe H, Igarashi T, Hong Z, Kido J. Squaraine dyes for organic photovoltaic cells. *J Mater Chem a*. 2015;3:14517-14534.
- Gambino S, Mazzeo M, Genco A, et al. Exploring light-matter interaction phenomena under ultrastrong coupling regime. *ACS Photonics*. 2014;10:1042-1048.
- Schulz M, Balzer F, Scheunemann D, et al. Chiral excitonic organic photodiodes for direct detection of circular polarized light. *Adv Funct Mater*. 2019;29:1900684.
- Abdullaeva OS, Balzer F, Schulz M, et al. Organic Photovoltaic Sensors for Photocapacitive Stimulation of Voltage-Gated Ion Channels in Neuroblastoma Cells. *Adv Funct Mater*. 2019;29:1805177.
- Sun P, Wu Q, Sun X, et al. J-aggregate squaraine nanoparticles with bright NIR-II fluorescence for imaging guided photothermal therapy. *Chem Commun*. 2018;54(95):13395-13398.
- Brandt JR, Salerno F, Fuchter MJ. The added value of small-molecule chirality in technological applications. *Nat Rev Chem*. 2017;1:1-12.
- Di Nuzzo D, Kulkarni C, Zhao B, et al. High circular polarization of electroluminescence achieved via self-assembly of a light-emitting chiral conjugated polymer into multidomain cholesteric films. *ACS Nano*. 2017;11(12):12713-12722.
- Balzer F, Kollmann H, Schulz M, et al. Spotlight on excitonic coupling in polymorphic and textured anilino squaraine thin films. *Cryst Growth des*. 2017;17:6455-6466.
- Viterisi A, Montcada NF, Kumar CV, et al. Unambiguous determination of molecular packing in crystalline donor domains of small molecule solution processed solar cell devices using routine X-ray diffraction techniques. *Mater Chem a*. 2014;2:3536-3542.
- Tristani-Kendra M, Eckhardt CJ. Influence of crystal fields on the quasimetallic reflection spectra of crystals: optical spectra of polymorphs of a squarylium dye. *J Chem Phys*. 1984;81:1160-1173.
- Chen G, Sasabe H, Lu W, et al. J-aggregation of a squaraine dye and its application in organic photovoltaic cells. *J Mater Chem C*. 2013;1:6547-6552.
- Deing KC, Mayerhöffer U, Würthner F, Meerholz K. Aggregation-dependent photovoltaic properties of squaraine/PC61BM bulk heterojunctions. *Phys Chem Chem Phys*. 2012;14(23):8328-8334.

21. Lambert C, Koch F, Völker SF, et al. Energy transfer between squaraine polymer sections: from Helix to zigzag and all the way back. *J Am Chem Soc.* 2015;137(24):7851-7861.
22. Hestand NJ, Zheng C, Penmetcha AR, et al. Confirmation of the origins of panchromatic spectra in squaraine thin films targeted for organic photovoltaic devices. *J Phys Chem C.* 2015; 119:18964-18974.
23. Paternò GM, Moretti L, Barker AJ, et al. Near-infrared emitting single squaraine dye aggregates with large Stokes shifts. *J Mater Chem C.* 2017;5:7732-7738.
24. Zhong C, Bialas D, Collison CJ, Spano FC. Davydov splitting in squaraine dimers. *J Phys Chem C.* 2019;123:18734-18745.
25. Stoll RS, Severin N, Rabe JP, Hecht S. Synthesis of a novel chiral squaraine dye and its unique aggregation behavior in solution and self-assembled monolayers. *Adv Mater.* 2006;18:1271-1275.
26. Arteaga O, Ossikovski R. Complete Mueller matrix from a partial polarimetry experiment: the 12-element case. *JOSA a.* 2019; 36:415-416.
27. Arteaga O, Kuntmann E, Antó J, Pascual E, Canillas A, Bertran E. Mueller matrix microscopy on a Morpho butterfly. *J Phys: Conf Ser.* 2015;605:012008.
28. Burkhardt A, Pakendorf T, Reime B, et al. Status of the crystallography beamlines at PETRA III. *Eur Phys J Plus.* 2016;131:56.
29. Kabsch W. XDS. *Acta Crystallogr Sect D.* 2010;66:125-132.
30. Sheldrick GM. SHELXT – integrated space-group and crystal-structure determination. *Acta Crystallogr Sect a.* 2015;71:3-8.
31. Sheldrick GM. Crystal structure refinement with SHELXL. *Acta Crystallogr Sect C.* 2015;71:3-8.
32. Hübschle CB, Sheldrick GM, Dittrich B. ShelXle: a Qt graphical user interface for SHELXL. *J Appl Cryst.* 2011;44(Pt 6):1281-1284.
33. Rigaku Oxford Diffraction. *CrysAlisPro Software system version 38.46.* Oxford, UK: Rigaku Corporation; 2018.
34. Dolomanov OV, Bourhis LJ, Gildea RJ, Howard JAK, Puschmann H. OLEX2: a complete structure solution, refinement and analysis program. *J Appl Cryst.* 2009;42:339-341.
35. Balzer F, Schiek M, Osadnik A, et al. Substrate steered crystallization of naphthyl end-capped oligothiophenes into nanofibers: the influence of methoxy-functionalization. *Phys Chem Chem Phys.* 2014;16(12):5747-5754.
36. Balzer F, Schiek M. Automated polarized microscopy analysis of fluorescent and birefringent nano- and microfibers. In: Müller SCM, Parisi J, editor. *Bottom-Up Self-Organization in Supramolecular Soft Matter.* Berlin: Springer; 2015. p151-176.
37. Brück S, Krause C, Turrisi R, et al. Structure-property relationship of anilino-squaraines in organic solar cells. *Phys Chem Chem Phys.* 2014;16(3):1067-1077.
38. Hestand NJ, Spano FC. Expanded theory of H- and J-molecular aggregates: the effects of vibronic coupling and intermolecular charge transfer. *Chem Rev.* 2018;118(15):7069-7163.
39. Lindorfer D, Renger T. Theory of anisotropic circular dichroism of excitonically coupled systems: application to the baseplate of green sulfur bacteria. *J Phys Chem B.* 2018;122(10): 2747-2756.
40. Kuball HG, Dorr E, Hoefler T, Tuerk O. Exciton chirality method. Oriented molecules-anisotropic phases. *Monatshfte für Chemie.* 2005;136:289-324.
41. Tellegen BDH. The gyrator, a new electric network element. *Philips Res Rept.* 1948;3:81-101.
42. Ossikovski R, Arteaga O. Extended Yeh's method for optically active anisotropic layered media. *Opt Lett.* 2017;42(18):3690-3693.
43. Luft M, Groß B, Schulz M, Lützen A, Schiek M, Nilius N. Adsorption of squaraine molecules to Au(111) and Ag(001) surfaces. *J Chem Phys.* 2018;148:074702.
44. Pescitelli G, di Bari L, Berova N. Application of electronic circular dichroism in the study of supramolecular systems. *Chem Soc Rev.* 2014;43(15):5211-5233.
45. van Dijk L, Bobbert PA, Spano FC. Extreme sensitivity of circular dichroism to long-range excitonic couplings in helical supramolecular assemblies. *J Phys Chem B.* 2010;114(2): 817-825.
46. Gentile MJ, Núñez-Sánchez S, Barnes WL. Optical field-enhancement and subwavelength field-confinement using excitonic nanostructures. *Nano Lett.* 2014;14(5):2339-2344.
47. Zheng C, Zhong C, Collison CJ, Spano FC. Non-Kasha behavior in quadrupolar dye aggregates: the red-shifted H-aggregate. *J Phys Chem C.* 2019;123:3203-3215.
48. Nye JF. *Physical Properties of Crystals: Their Representation by Tensors and Matrices.* Oxford: Oxford University Press; 1985: 352p.

SUPPORTING INFORMATION

Additional supporting information may be found online in the Supporting Information section at the end of this article.

How to cite this article: Zablocki J, Arteaga O, Balzer F, et al. Polymorphic chiral squaraine crystallites in textured thin films. *Chirality.* 2020; 32:619–631. <https://doi.org/10.1002/chir.23213>